Multiscale modeling of grain boundaries in ZrB_2: structure, energetics, and thermal resistance

John W. Lawson*

Thermal Protection Materials Branch, Mail Stop 234-1,

NASA Ames Research Center, Moffett Field, CA 94035

Murray S. Daw

Department of Physics and Astronomy,

Clemson University, Clemson, SC 29631

Thomas H. Squire

Thermal Protection Materials Branch, Mail Stop 234-2,

NASA Ames Research Center, Moffett Field, CA 94035

Charles W. Bauschlicher, Jr.

Entry Systems and Technology Division, Mail Stop 230-2,

NASA Ames Research Center, Moffett Field, CA 94035

Abstract

A combination of *ab initio*, atomistic and finite element methods (FEM) were used to investigate the structures, energetics and lattice thermal conductance of grain boundaries for the ultra high temperature ceramic ZrB_2. Atomic models of idealized boundaries were relaxed using density functional theory. Information about bonding across the interfaces was determined from the electron localization function. The Kapitza conductance of larger scale versions of the boundary models were computed using non-equilibrium molecular dynamics. The interfacial thermal parameters together with single crystal thermal conductivities were used as parameters in microstructural computations. FEM meshes were constructed on top of microstructural images. From these computations, the effective thermal conductivity of the polycrystalline structure was determined.

*Electronic address: John.W.Lawson@nasa.gov

I. INTRODUCTION

Ultra high temperature ceramics (UHTC) are a class of materials with high melting points, good mechanical properties and reasonable oxidation resistance. Among these materials, the metallic diborides, and especially ZrB_2, have been the object of considerable study, both as pure materials and as constituents in composites. These materials are of interest for applications in extreme environments which require little or no oxidation or ablation. In particular, they are candidate materials for sharp leading edges and nosecaps of hypersonic aircraft as well as propulsion systems, refractory crucibles, among other applications [1–4]. Unlike most ceramics, UHTCs are distinguished by their high thermal conductivity. High thermal conductivity offers a number of advantages for high temperature applications. For example, high thermal conductivity can improve thermal shock resistance. It can also improve the efficiency of thermal radiation by rapidly redistributing thermal energy across available surfaces.

The total thermal conductivity κ_{tot} of the diborides has significant contributions from both electronic and lattice carriers [5]. The electronic component κ_e can be estimated approximately from knowledge of the electrical conductivity σ using the Weidemann-Franz (WF) empirical relation, $\kappa_e = \kappa_0 \sigma T$, where κ_0 is the Lorentz constant ($2.45 \times 10^{-8} W \cdot \Omega \cdot K^{-2}$) and T is the temperature. The lattice contribution κ_{ph}, which results from phonon transport, cannot be measured directly and is usually inferred by subtracting κ_e from κ_{tot}. While not accessible to experimental measurement, the bulk lattice thermal conductivity as well as the lattice thermal resistance of grain boundaries can be determined directly from molecular dynamics (MD) simulations.

For single crystal ZrB_2, thermal conductivity measurements at room temperature have been reported as $140 W/(m \cdot K)$ in the basal direction and $100 W/(m \cdot K)$ along the c-axis [6]. These single sample results did not include either a characterization of the defect distribution, which will reduce κ_{tot}, or specific estimates of κ_e and κ_{ph}. Polycrystalline ZrB_2 has been more thoroughly studied. Previously, room temperature measurements have been reported as $55 W/(m \cdot K)$ for ZrB_2 where κ_e was estimated to be $33 W/(m \cdot K)$ using the WF relation and κ_{ph} was given as $22 W/(m \cdot K)$ [7]. More recent results [8] quote values as high as $108 W/(m \cdot K)$. The reduction of κ_{tot} relative

to single crystals comes primarily from the thermal resistance of grain boundaries. Variations of κ_{tot} with grain size can be substantial [7, 8]. While κ_e is expected to be relatively insensitive to grain boundaries due to the short electron mean free path, the lattice contribution κ_{ph}, which may be quite high in single crystals, can be reduced significantly due to grain boundary thermal resistance [7]. Different processing methods can lead to very different grain sizes and grain boundary structures. Therefore, it is important to understand the effect of grain boundaries on the properties of these materials.

In this paper, we use a multiscale approach to model structure-property relationships in polycrystalline ZrB_2. We focus primarily on thermal properties; however our results also have implications for mechanical response. To start, *ab initio* methods were used to examine the structure and energetics of simple grain boundary structures, namely coincidence and near coincidence *tilt* and *twist* boundaries. Relaxation of these interfaces leads to significant reconstruction of the atomic arrangement and also of the bonding across the interfaces. Thermal resistance of the boundaries was computed with nonequilibrium molecular dynamics using recently derived interatomic potentials for this material [9]. Previously, the lattice thermal conductivity of single crystal ZrB_2 was computed using these same potentials [10]. Thermal conductivity parameters from the atomistic simulations were used in microstructural calculations to determine the reduction in thermal conductivity due to the grain boundary network. Finite element method (FEM) computations were performed where FEM meshes were constructed directly on scanning electron microscopy (SEM) images. From these computations, the "effective thermal conductivity" of the polycrystalline microstructure could be determined.

II. METHOD

Ab initio computations were performed in the context of density functional theory (DFT) utilizing the functional of Perdew, Burke, and Ernzerhof (PBE) [11]. This functional is known to give good results especially for solids. *Ab initio* methods were used to relax the grain boundary structures and to evaluate their energetics. *Ab*

initio results were compared to results obtained from the interatomic potentials to help assess the accuracy of those potentials. The plane wave code VASP was used for all calculations [12]. The Projected Augmented Wave (PAW) potentials were employed. All results were converged with respect to k-point sampling and plane wave energy cutoff E_c. Because of the large unit cells considered, small k-space meshes were sufficient. Typically, $2x2x2$ meshes were used for larger systems and $6x6x6$ meshes for smaller unit cells. Energy cutoffs were typically about $400eV$.

Information about bonding was obtained from the electron localization function (ELF) [13, 14]. The ELF gives the probability of finding an electron near a reference electron at a given point and with a fixed spin. In this way, it is useful for identifying covalent bonds. The ELF is defined in terms of a dimensionless localization ratio $\chi_\sigma(r)$ which measures localization with respect to the uniform electron gas

$$ELF(r) = \frac{1}{1+\chi_\sigma^2(r)}. \tag{1}$$

The ELF takes values in the range $0 \leq ELF \leq 1$ where $ELF = 1$ corresponds to perfect localization and $ELF = 0.5$ gives the electron gas. $\chi_\sigma(r)$ is computed directly from DFT quantities. The ELF can be contrasted against the electron charge density $\rho(r)$ which is a single electron quantity whereas the ELF gives information about the two-body distribution.

Nonequilibrium molecular dynamics (MD) simulations were performed with the $LAMMPS$ package [15] and using the interatomic potentials for ZrB_2. The method of Muller-Plathe (MP) was used to compute interfacial thermal conductances [16–18]. Periodic unit cells with a long direction normal to the boundaries were created. Periodicity results in two boundaries per cell. NVE simulations were performed in which a "hot" region and a "cold" region were created on opposite sides of the boundaries by exchanging atoms between the two regions: the atom with the greatest kinetic energy in the cold region is swapped with the lowest kinetic energy atom in the hot region. After a steady state is established, a temperature gradient between the regions, and across the interfaces, resulted where the heat flux Q is given by

$$Q = \frac{1}{2tA}\sum_i \frac{m}{2}(v_{i,hot}^2 - v_{i,cold}^2) \tag{2}$$

where the sum is over the number of exchanges, t is the total simulation time, A is the cross-sectional area normal to the direction of heat flow, m is the atomic mass and v_i is the velocity of the exchanged atom. Near the sink/source regions, the temperature profile is nonlinear. For a homogeneous system however, i.e. without any interfaces, a linear region between the sink/source will develop whose slope obeys Fourier's Law. In the presence of an interface, a grain boundary, for example, a discontinuity in the temperature profile will appear at the interface. The temperature discontinuity and the exchanged heat flux are related by the interfacial or Kapitza conductance σ_K

$$Q = \sigma_K \Delta T. \tag{3}$$

where the inverse of the Kapitza conductance is the Kapitza resistance $R_K = 1/\sigma_K$.

Simulations were performed using the recently derived ZrB_2 interatomic potentials of Daw, Lawson and Bauschlicher (DLB) [9]. Two sets of potentials were reported: "Pot 1" and "Pot 2". Subsequently, in lattice thermal conductivity simulations [10], Pot 2 was found to give an normal conductivity that was greater than the in-plane value, a result that contradicted the experimental ordering. Pot 1 however gave generally good results including the correct ordering. For that reason, in this work, we focus on Pot 1 only.

Simulations were performed as follows. Normal to the interfaces (z-direction), the unit cells had dimensions on the order of $100nm$ to minimize reflections from the boundaries. Results were only weakly dependent on the lateral dimensions, however, which was typically ($\sim 1 - 5nm$). Convergence studies for both the normal and lateral dimensions were performed. Initial velocities were generated from a gaussian distribution. A NPT simulation was run at the given temperature for $100ps$ to equilibrate the system. Time steps of $1fs$ were typically used. Next, particle swapping according to the Muller-Plathe algorithm was performed; steady state was typically well-established after $500ps$. Temperature profiles (T vs z) were determined by dividing the system into narrow slices perpendicular to the long direction of the system, i.e. parallel to the grain boundaries. Within each slice, the local temperature was evaluated. Steady state temperature profiles were determined by averaging the temperatures in each slice over runs of $4ns$. The temperature discontinuity across the

interface was determined by fitting linear functions on opposite sides of the discontinuities and evaluating the temperature drop at the interface.

Finite element computations were performed using the open source code $OOF2$ [19] and the commercial code $MSCMarc$ [20]. Finite element meshes were constructed directly on an SEM image of the microstructure of ZrB_2 [3]. $OOF2$ contains image processing and mesh generation algorithms especially suited for imaged based FEM. $MARC$ was used to perform the FEM computations because of its more extensive computational capabilities. FEM meshes were created for both the grains and the boundaries, each of which was treated as a separate material with distinct thermal conductivities. Thus, the grain boundaries are treated as an "interphase". FEM interface computations are often performed using boundary elements however $OOF2$ does not currently have that capability. The two descriptions are expected to be equivalent.

The effective thermal conductivity κ_{eff} of the full microstructure (grains + boundaries) was evaluated in three different ways. First, a transient thermal analysis was performed where a thermal flux was applied to one side of the system while the other sides were maintained as adiabatic boundaries. The temperature of the opposing side of the system (the "backface") was determined as a function of time. The κ_{eff} of the full polycrystal was evaluated by performing a second transient thermal analysis on an equivalent, homogeneous, reference material. The thermal conductivity of the reference was tuned to give a backface temperature trace that matched the polycrystalline result.

Next, we performed a steady state thermal analysis using two different sets of boundary conditions. First, a uniform temperature gradient (UTG) was applied by fixing the temperature of opposite sides of the model. A transient thermal analysis was performed until the system reached steady state. Second, we applied a uniform heat flux (UHF) to opposites sides of the system until a steady state was reached. For both cases, UTG and UHF,

$$< q >= -\kappa_{eff} \cdot < \nabla T > \tag{4}$$

where q is the heat flux, κ_{eff} is the effective thermal conductivity, ∇T is the temperature gradient and the brackets represent volume averages over the system. Note

for UTG, we fix ∇T and measure $< q >$ after steady state is achieved. For UHF, we do the converse. Both methods were performed with boundary conditions applied in both the vertical and horizontal directions as well. It has been shown that $\kappa_{UHF} < \kappa < \kappa_{UTG}$ [21].

A fundamental question in evaluating the effective properties of heterogeneous, microstructural models is whether the model is representative of the bulk system [22, 23]. It has been suggested that a model can be considered representative if its response to different boundary conditions, such as UTG and UHF, is the same. Thus, any microstructure above some minimal size will yield the same effective properties independent of boundary conditions, i.e. the bounds on κ are very tight. If the model is too small, i.e. it is not representative, different boundary conditions will give different effective properties.

III. STRUCTURAL MODELS

The single crystal structure of ZrB_2 is the AlB_2-type, designated as $C32$ with space group symmetry *P6/mmm*. This is a layered arrangement with alternating planes of pure Zr and pure B atoms. The Zr atoms are transition metals and are considerably larger than the B atoms both in terms of atomic radii and also mass. The Zr atom has a mass of 91.2 g/mol and an atomic radii of 1.6Å while Boron is a relatively small atom with an atomic radius of 0.9Å and an atomic mass of 10.8 g/mol. The Zr planes have a hexagonal close packed structure while the B planes are open, hexagonal with six membered rings resembling graphite. The layers are situated such that each Zr atom lies directly above and below the centers of 6-membered B rings in the adjacent planes. The primitive cell of these structures contains one formula unit (one Zr and two Bs) and the crystal has simple hexagonal symmetry (D_{6h}). The lattice constant "a" gives the metal-metal atom distance within a plane and the "c" lattice constants give the metal-metal atom distance in alternate planes. The a and b axes are symmetry-equivalent, in-plane directions while the c axis is normal to planes.

Structural models for ZrB_2 grain boundaries are considered for four situations: two twist boundaries and two tilt boundaries, one for each of the two independent

axes, a and c. Hexagonal crystals with irrational ratios of their lattice parameters $(c/a)^2$ only have exact coincidence site lattice (CSL) boundaries corresponding to rotations about the c-axis [24–26]. We consider such CSL boundaries formed by twists and tilts about that axis. However, near coincidence boundaries about the a-axis can be formed by approximating $(c/a)^2$ as an rational number (m/n). This approximation will introduce a strain into the system. Smaller (n, m) values result in smaller, computationally efficient unit cells, but with larger strain. For larger values, the converse is true. For our structures, the strain was typically less than 1%. To accommodate *ab initio* computations, periodic cells were used, containing two boundaries per cell. With small cells, we expect nontrivial interaction between the boundaries. However we should be able to obtain reliable information about relative structural and energetic differences.

For ceramics such as ZrB_2, grain boundaries are often disordered and may contain many impurities. However, such boundaries are usually the result of particular processing methods. Cleaner and more crystalline boundaries are expected to have low interfacial energies and therefore their formation should be favored with improved processing methods. Further, such boundaries should have greater interfacial adhesion and reduced thermal resistance, and therefore are more desirable. Such boundaries are routinely observed in other ceramics such as alumina and zirconia [27, 28]. In this paper, we focus on these relatively simple boundaries both because of their computational efficiency and also because of their expected superior properties. We expect grain boundary thermal properties to be somewhat insensitive to the exact atomic structure of the boundary. Therefore, it is not necessary to find the absolute, lowest energy boundary structure, which can be a highly nontrivial task as has been shown in recent work [29, 30] and is beyond the scope of this paper.

A. C-tilt

The first boundary we consider is a $\Sigma 7$ symmetric tilt around the c-axis. This exact CSL boundary is shown in Fig 1. As a shorthand we refer to this boundary as "c-tilt". Because the Boron sublattice in ZrB_2 is graphitic, we propose a c-tilt grain

boundary structure in analogy with graphite. Related structures have been recently proposed for graphene [31, 32]. The boundary consists of a sequence of five and seven (5-7) membered Boron ring units that are separated by hexagonal rings. The distance between these units is related to the tilt angle where lower angles correspond to a larger separation between the 5-7 pairs. The smallest such structure is the $\Sigma 7$ structure. To complete the structure for ZrB_2, Zr atoms are positioned over/above all Boron rings including the 5 and 7-membered rings. This structure can also be viewed as an array of edge dislocations with a horizontal Burger's vector where the five membered rings represent the extra plane of atoms.

B. C-twist

The second boundary is a $\Sigma 7$ symmetric twist about the c-axis. We call this boundary "c-twist" and it is displayed in Fig 2. This boundary is the simplest of the ones we will consider and shows the least reconstruction. The interface structure has a layer of Zr and a layer of B shifted relative to each other. Thus, across the interface, the Zr atoms are not centered directly above and below Boron 6-membered rings. This twist results in a small degree of crumpling of the two layers, mainly in the Boron layer. However, large scale reconstruction does not occur because the intralayer interactions (metallic Zr and covalent B) have not been disturbed significantly. The interfacial layers also are further stabilized by the compounded effect of additional layers away from the boundary.

C. A-tilt

The third structure we consider is a 90°, near coincidence, asymmetric tilt boundary about the a-axis, which we call "a-tilt". This model contains two boundaries, which we designate Left and Right, as shown in Fig 3. This configuration has atomic layers oriented perpendicular to each other. With respect to the Boron layers, the Left and Right boundaries are mirror images of each other. Namely, flat, vertical, graphitic sheets of Borons (the outer sections of Fig 3) interact with Boron edge configurations (the inner section of Fig 3). This mirror symmetry is broken however by

Zr layers inserted into the two boundaries. A rotated view of this structure can be seen in Fig 7.

For the Left boundary, the inserted Zr layers match the middle section Boron layer. However, a deficit of Zr atoms now exists to match the Boron layer to the left. Recall the Zr atoms want to be positioned inside a Boron 6-membered ring. This is only possible for the top and bottom Zr atoms in the Left boundary of Fig 7, leaving the middle two Zr atoms to share three Boron rings. As expected, the Boron rings with the perfect Zr match remain nearly flat, however the next, neighboring ring crumples slightly due to the two, off-center, middle Zr atoms. The next ring, on the other hand, is flat again as a result of a balancing between the two, off-center Zr atoms. This is somewhat surprising since there are not two Zr atoms centered on opposite sides of this ring. Thus, we find an alternating structure of flat and crumpled Boron rings in the Left interface.

For the Right boundary, the Zr sheet matches perfectly the Boron layer to its right. However, there are too many Zr atoms in this layer to match the edge Boron layers on its left. These extra Zr atoms produce considerable crowding of the middle section Borons as can be seen in Fig 7. In fact, we see that every fourth Zr atom lines up "eye-to-eye" with a edge-on Boron sheet. These "edge-on" Zr atoms compress the other three Zr so that they cannot line-up with the Zr sheets in the middle section. This Zr compression has an effect on the Boron sheets which are bent up or down at their edges.

D. A-twist

The final boundary is a 90°, near coincidence, asymmetric twist about the a-axis, which we designate "a-twist". There are important similarities between a-twist and a-tilt. Fig 4 shows the periodic model for a-twist with two boundaries, denoted Left and Right. Both Left and Right boundaries have two sets of 90° rotated edge-on Boron planes interacting with each other.

With the Left boundary, the plane of Zr atoms matches the layering sequence of the middle section of the structure. However, the edge-on Boron planes to the right

of the interface want a Zr fitted into each well of the zig-zag Boron configuration. On the Left boundary, therefore, there is one Zr atom too few per repeat unit, leaving an effective Zr vacancy in the center of the boundary. This results in a complicated 4-membered Boron ring configuration. Above and below this ring, Zr atoms are pushed away, resulting in the bending of both Zr and B planes near that boundary.

The Right interface is different in that the plane of Zr atoms matches precisely the edge-on Boron planes to the left of the boundary. However, there is an extra Zr atom (actually a column of Zr going into the page of the figure) in this layer relative to the middle section where the Zr atoms want to be positioned between the Boron layers. The extra Zr atom, however, creates the same situation as a-tilt in that the Zr atom is effectively attached to the end of a Boron plane. Zr atoms above and below this atom are pushed away causing bending of the middle planes as they approach the boundary. We can see in the Boron plane that is edge-on to the extra Zr atom that the Boron rings are compressed along that edge. A rotated version of this exact situation is seen in the Left boundary where a line of edge-on Borons has been pushed back behind the main part of the boundary. This column of Borons has been compressed by an extra column of Zr that is vertical to the figure on the Left boundary.

While a-twist and a-tilt have similar features, a-twist appears more disordered than a-tilt. This is a result of how the Boron planes interact with each other across their respective boundary. For a-tilt, the Boron planes on the left of the Left boundary and on the right of Right boundary are flat, chemically unreactive with no dangling bonds. The middle section of a-tilt has exposed edge-on Borons that could be reactive, but they are separated from the unreactive sheets by layers of large Zr atoms. For a-twist, the Boron sheets on both sides of both boundaries have the more reactive, edge-on configuration. This permits nontrivial Boron-Boron bonding across the interface and therefore a denser boundary. We will have more to say about this when we examine the electronic structure.

IV. ELECTRONIC STRUCTURE

The electronic structure of single crystal ZrB_2, and the related material HfB_2, was discussed in detail in a previous publication [33]. Here we summarize some of those results. The electronic configuration for Zr is $[Kr]5s^24d^2$. Thus, this species has two "s" and two "d" valence electrons to donate to the material. Boron's electronic configuration is $[He]2s^22p^1$, giving it one less valence electron than Carbon. This electron "deficiency" has a significant impact on the properties of pure Boron whose ground state structure is still unresolved. In pure materials, Boron is known to form strong covalent bonds.

Despite its simple atomic structure, ZrB_2 displays all three major electronic bonding motifs. Namely, the bonding in the Zr planes is metallic; the bonding in the B planes is covalent; and the bonding between layers is ionic. In the metallic Zr layers, the electron localization function (ELF) is diffuse and relatively non-localized. ELF accumulation points however were found in the Zr planes positioned at the center of the Zr triangles. Thus these points formed six-member rings in the Zr plane. Interestingly, the accumulation points appear above/below Boron atomic sites in the neighboring planes. It is possible that the interaction between the Zr electron density at the ELF accumulation points and the Boron density determines the nature of the interlayer bonding. In the B planes, the electrons are well-localized into covalent, highly directional bonds between neighboring B atoms. This is reflected in high ELF values between neighboring Boron atoms. Between layers, significant charge transfer was found as electron "rich" Zr layers donated electronic charge to the electron "deficient" B layers.

The electronic structure of grain boundaries can provide important information that impact interface properties [34, 35]. The formation of an interface may result in significant reconstruction of the boundary atomic structure. The accompanying changes to the electronic structure can result in the formation of localized electronic states at the boundary as well as significant modifications to the bonding across the boundary. A range of scenarios is possible from the formation of dangling bonds to strong covalent bonding across the interface. The nature of the interfacial bonding

will affect boundary properties such as adhesion, formation energies, and thermal conductance, among others.

A. C-tilt

In Fig 5 we show the ELF for c-tilt. C-tilt is one of the least disrupted boundaries. The material is still layered in the same way as with the single crystal, but at the boundary, 5-7 ring pairs are inserted which results in the different crystal orientation on either side of the boundary. The ELF clearly shows the same bonding motifs survive the formation of this boundary, namely there is covalent bonding in the Boron planes including among the 5-7 rings. Region of high ELF are seen between all Boron pairs regardless of the ring type (5-,6-,7-membered rings). Interesting, the 5-7 rings remain flat without crumpling. Because of the strong covalent bonding across this interface, we expect especially strong interfacial adhesion and thermal conductance for this boundary.

B. C-twist

The bonding structure for c-twist is relatively simple. The crystal structure on either side of the boundary remains intact except at the interface where a Boron and a Zirconium layer have been shifted relative to each other. We display the ELF for the boundary in Fig 6. In particular, we consider the ELF in the plane on the Zr side of the boundary. This particular plane is sandwiched between two Boron planes. In the single crystal, the Boron planes are mirror images and the Zr ELF forms accumulation points in an open hexagonal lattice that corresponds to the locations of the Borons in the two neighboring planes. In the case of c-twist however the Boron in the two neighboring planes are shifted relative to each other. Therefore, the ELF accumulation points in the Zr plane no longer line up with the Boron atoms across the interface. The implication of this is not completely clear, but it is expected that this mismatch will weaken the ionic bonding across the interface.

C. A-tilt

In Fig 7, the ELF for a-tilt is shown in a plane crossing the boundary where the orientation has been rotated with respect to Fig 3. Fig 7 shows a contour slice where blue is high ELF (> 0.5), green is low ELF (< 0.5) and white is close to 0.5. As with Fig 3, this cell has two asymmetric grain boundaries, Left and Right. The middle section of the Figure has horizontal layers while the left and right sections have vertical layers, reflecting the 90° tilt of the two boundaries. The ELF plane displayed in Fig 7 contains only Boron atoms on both sides of the interfaces. The Zr atoms in the Figure are in front of the contour plane. The plane that is displayed has the maximum ELF at the interface. High ELF in ZrB_2 is associated principally with the Boron sublattice where covalent bonding exists between Boron atoms. Thus, pockets of high ELF result from pairs of Boron atoms and indicate possible covalent bonding across the boundary.

As discussed previously, the Left boundary is an interface between a flat, vertical Boron layer and the neighboring Zr layer to the right. The Zr layer in this interface has missing atoms with respect to the Boron layer, and therefore not enough Zr atoms match with the Boron rings to the left. The bonding across this boundary is expected to be ionic due to the $Zr-B$ interaction However, we see evidence from the ELF plot of some non-trivial electron localization inside the interface involving pairs of B atoms. In Fig 7, the vertical Boron sheet to the left has three pockets of high ELF which line up with five pockets of high ELF from the horizontal sheets. These Boron ELF clouds are distorted slightly and may enhance the interaction across the interface. On the Right boundary, we have too many Zr atoms, and in fact, one column of the middle Zr (into the page of Fig 7) is partially surrounded by an "edge-on" Boron ring as opposed to hovering above or below. The Zr atoms above and below this edge-on Zr are pushed up and down causing corresponding bending of the Boron planes. From the ELF plot, pockets of localized electrons are also seen associated with B pairs atoms across the boundary. In this case, some of the B pairs have been distorted relative to their position on the Left boundary. The Right boundary is more complex than the Left boundary since there are Zr-Zr interactions

in addition to Zr-B and B-B interactions.

D. A-twist

In Fig 8, we show an ELF contour plot for a-twist; the plane displayed has the maximum ELF across the interfaces. As discussed previously, a-twist is an asymmetric configuration and therefore the Left and Right boundaries are different. Due to the reactive edge-on Boron plane interacting at both interfaces, a-twist has complex bonding across its boundaries. A central exotic feature of this structure is the horizontal Boron plane in the center of the middle section of Fig 8. This Boron plane intersects the two boundaries in very different ways. At the Left boundary where there are missing Zr atoms, 4-membered covalent Boron rings form. The ELF shows that there is strong covalent bonding in this ring that reaches across the Left interface. At the Right boundary, the same Boron plane encounters an extra Zr atom at that interface. As as result, this particular Boron plane is compressed relative the other Boron planes. There is strong covalent bonding across both Left and Right interfaces, resulting from 6-membered rings twisted at 90° relative to each other across the interfaces, but still covalently bonded to each other. In addition, most of the Zr atoms in both boundaries are surrounded by Boron structures on five sides, instead of the single crystal configuration with Borons only above and below the Zr. Thus, there is non-trivial and complex electronic structure between these Zr and their Boron rich caged structures.

V. GRAIN BOUNDARY ENERGETICS

The grain boundary interfacial excess energy was defined as

$$\gamma = (E_{GB} - nE_{bulk})/2A \tag{5}$$

where E_{GB} is the total energy of the grain boundary cell, E_{bulk} is the total energy of a formula unit of single crystal bulk material, n is the number of formula units to match the number of atoms in the grain boundary cell, and A is the area of the

interface. The factor of "2" is because there are two boundaries per periodic cell. The volume of the interface defined was as

$$\Delta_z = (z_{GB} - z_{bulk})/2 \tag{6}$$

where z_{GB} is the length of the relaxed cell in the direction normal to the boundary and z_{bulk} is the length of an equivalent cell with no boundary.

These quantities were calculated for unit cells corresponding to the structures shown in Fig 1-4 using *ab initio* computations and also using the ZrB_2 interatomic potentials. The results are shown in Table I. With such small cells (from 72 atoms for *a*-tilt to 1344 atoms for *a*-twist), significant interactions is expected between the two boundaries in each cell. As previously discussed, *c*-tilt and *c*-twist are exact CSL boundaries whereas *a*-tilt and *a*-twist are near CSL structures. The near CSL interfaces have a small amount of artificial strain (less than 1%). To maintain these structures, their volume was fixed during the optimization and only the ionic positions were allowed to relax. Because of the fixed volume, Δ_z will necessarily be zero for these cases. Both of these factors, interface interactions and unit cell strain, will affect our results in absolute terms however relative differences can be considered. In addition, comparison with *ab initio* results will help access the accuracy of these new potentials.

In Table I, the relaxed and unrelaxed (in parenthesis) interfacial energies are given. The amount of relaxation in the energy is related to the degree of reconstruction of the structures. *C*-tilt and *c*-twist have the lowest interfacial energies with 153 meV/Å^2 and 157 meV/Å^2, respectively, compared to 227 meV/Å^2 for *a*-tilt and 212 meV/Å^2 for *a*-twist. *A*-tilt and *a*-twist have considerably more reconstruction compared to *c*-tilt and *c*-twist as indicated by the significant relaxation in these structures. It is somewhat surprising that *a*-tilt has a higher energy than *a*-twist since *a*-twist is more disordered. However, the significant covalent bonding across the *a*-twist interfaces may be a factor in reducing its energy relative to *a*-tilt. The results for *c*-tilt and *c*-twist are consistent with the intuition that they are the least reconstructed structures and therefore should be the easiest to form. They are also low Σ CSL boundaries and therefore are expected to have low energies. An *ab initio* number for Δ_z can only be evaluated for *c*-twist and that value is 0.29Å.

Interfacial energies from the interatomic potential are very similar among the boundaries, with a variation of a few percent. Results are consistently lower for the potentials compared to the *ab initio* numbers, in the case of a-tilt and a-twist by a factor of 2X. The highest energy from the potentials is 118 meV/Å^2 for a-twist and the lowest is 107 meV/Å^2 a-tilt. Given the similarity of these numbers, it is difficult to establish a clear ordering. However, the degree of relaxation is consistent with the *ab initio* results with a much small amount of relaxation for c-tilt and c-twist compared to a-tilt and a-twist. The results for Δ_z for c-twist agrees very well with the *ab initio* number. It is clear however that the DLB potential does better for unrelaxed energies than relaxed. In fact, the expected ordering of the relaxed boundaries, as suggested by the *ab initio* results, are not well reproduced by DLB.

VI. THERMAL RESISTANCE

In Table I, we also present values for the thermal conductance of each boundary. These calculations were all performed at 300K. As discussed previously, the values were evaluated by creating a thermal gradient across the boundaries and evaluating the magnitude of the discontinuity at the interfaces. Thermal profiles for the four boundaries are shown in Fig 9. Unit cells with long dimensions normal to the boundary were used. These cells were typically more than $200nm$ in length to minimized reflections. The longest cell had of length of $248nm$ for c-twist. A-twist which had an unusually large lateral cross-section was the smallest at $109nm$ in length. Note that c-tilt and c-twist are symmetric boundaries whereas a-tilt and a-twist are asymmetric. Therefore, if the two boundaries in a unit cell are symmetric, they will both have same σ_K. In the asymmetric case, they can be different as indicated in the Table.

Some degree of correlation is expected between the interfacial energy γ and the thermal conductance σ_K. In particular, boundaries with low γ should have high σ_K. The variation among the σ_K values however is much greater than the variation among γ values from the potentials. Thus, establishing a clear relation is not obvious. However, the σ_K values do correspond to our intuition for these structures. C-tilt has the highest conductance with 1.77 $GW/(K \cdot m^2)$. The fact that c-tilt should have

a high thermal conductance is not surprising since the structural disruption of that boundary is relatively small and the strong covalent bonding across the boundaries should permit a smooth flow of thermal energy. A-twist and c-twist have very similar conductances with 0.55/0.53 $GW/(K \cdot m^2)$ and 0.58 $GW/(K \cdot m^2)$. Their γ values from the potentials are very similar however a much larger gap is seen in their *ab initio* γ values. A-tilt has the lowest conductances with values of 0.38/0.31 $GW/(K \cdot m^2)$ for the Left and Right boundaries. The a-tilt γ value is similar to a-twist at the *ab initio* level. However, we expect a-twist to have a higher thermal conductance than a-tilt because of the significant covalent bonding across that interface.

It is interesting that c-tilt which has a γ values on par with c-twist at the *ab initio* level has a much larger value for the thermal conductance σ_K. This may be due to the fact that thermal conductivity values are higher in-plane compared to normal directions. Therefore, in-plane interfacial conductances may be expected to be higher than for normal interfaces.

VII. MICROSTRUCTURAL MODELING

The effect of grain boundary networks on the bulk thermal conductivity of polycrystal ZrB_2 is now considered. To begin, a Brick Layer Model (BLM) is used to obtain an estimate for the reduction of thermal conductivity due to interfacial thermal resistance [36]. In the BLM, the effective thermal conductivity κ_{eff} is given by

$$\frac{1}{\kappa_{eff}} = \frac{1}{\kappa_0} + \frac{R_K}{d} \tag{7}$$

where κ_0 is the intrinsic lattice thermal conductivity of the material, R_K is the interfacial thermal resistance and d is the grain size. This expression states that the effective resistance is a sum of the intrinsic resistance plus the sum of the resistances for each boundary crossed. The relation estimates the reduction of thermal conductivity in a material from its intrinsic value due to interfacial resistance. The effective thermal conductivity κ_{eff} was evaluated using thermal parameters taken from our atomistic simulations. The value of κ_0 cannot be measured directly, therefore, we assigned a value of 50 $W/(m \cdot K)$ which was obtained from our previous atomistic computations

of the bulk lattice thermal conductivity of ZrB_2 [10]. This value is the average of the in-plane and normal conductivities obtained from those simulations. For R_K, we took the value for a-tilt which has the highest interfacial resistance of our structures, 3.3 $(m^2 \cdot K)/GW$. For d we used $6\mu m$ which is typical for these materials. The effective thermal conductivity κ_{eff} obtained was $48.6W/(m \cdot K)$ which represents a very small reduction in thermal conductivity from the intrinsic value. Experimental thermal conductivity values reported by Zimmerman *et al* [7] are around $22W/(m \cdot K)$ at room temperature. This suggests that the boundaries considered in this paper have very low interfacial thermal resistance compared to experimental data. This is not surprising since our structures are very pristine and current processing methods for ceramics typically give much more disordered boundaries with numerous impurities. On the other hand, this also shows that significant improvement in material properties can be obtained by improving the quality of the grain boundaries.

Next, to consider a more realistic microstructure than BLM, which assumes one dimensional conduction and a regular, evenly spaced grain boundary network, we evaluated κ_{eff} with FEM computations whose mesh was constructed on an SEM micrograph taken from Ref [3]. A FEM thermal analysis requires, in addition to a structure, parameters for the thermal conductivity, the specific heat and the density of the grains and the boundaries. For the density and the specific heat, we used bulk values as measured experimentally. For the thermal conductivity of the grains, we again assigned a value 50 $W/(m \cdot K)$. Since the MD interfacial resistances are significantly lower than what is expected for these materials, a more realistic value for σ_K was chosen to be 10.0 $MW/(m^2 \cdot K)$ [37]. To obtain an interphase conductivity κ_K, we multiply σ_K by a representative width and obtain $\kappa_K = 1W/(m \cdot K)$

The FEM transient analysis was performed as discussed previously. In Fig 10, we show the original SEM image, the FEM mesh, and the steady state temperature distribution in the material. As we can see, the conduction is not uniform as the grain boundary network impedes the flow, resulting in jagged thermal contours through the material. The effective thermal conductivity was determined by fitting the transient, temperature response at the bottom of the model to an equivalent homogeneous, reference material. Remarkably, the result for the effective thermal

conductivity of the material is 18 $W/(m \cdot K)$ which is very close to the experimental value of 22 $W/(m \cdot K)$. Transient temperature traces for the polycrystalline model and for the homogeneous, reference material are shown in Fig 11. The trace for a reference material with the intrinsic thermal conductivity κ_0 is also plotted to show the reduction in thermal conductivity. In addition to the transient computations, results from the UTG and UHF steady state computations are reported in Table II. The numbers agree very well with each other and with the transient conductivity indicating that this microstructural model is of sufficient size to be considered representative of a bulk system.

It is interesting to compare the FEM result with the BLM and also with the rule of mixtures using the same parameters. Using the BLM expression and the more realistic interfacial parameters, we obtain 10.1 $W/(m \cdot K)$ for κ_{eff}. This is a reasonable result since the BLM is a series resistance model and therefore should be lower than the FEM model which has both series and parallel contributions. Since the FEM model is a two phase system we can also apply the rule of mixtures which gives for this situation 44 $W/(m \cdot K)$. The rule of mixtures describes a system of parallel resistances, therefore it should give an upper bound for this model.

VIII. CONCLUSION

In this paper, we used a combination of *ab initio* computations, atomistic simulations and FEM calculations to study the structure and properties of grain boundaries and their impact on lattice thermal conductivity in ZrB_2. Four CSL and near CSL grain boundaries were considered. CSL boundaries are generally low energy structures with favorable properties. In particular, we considered tilt and twist boundaries relative to the c and a axes.

Ab initio methods and interatomic potentials were used to evaluate the energetics of these boundaries. In particular, *ab initio* results showed that the c-axis boundaries, c-tilt and c-twist, had lower interfacial energies than the a-axis boundaries, c-tilt and c-twist. The a-axis boundaries contained a small amount of intrinsic strain relative to the c-axis interfaces, but were also much more disordered as indicated by the

significant amount of relaxation. Energetics from the interatomic potential did not produce as clear an ordering, giving interfacial energies very similar to each other. The absolute values of the energies from the potentials were reasonable however. In addition, the degree of relaxation of the structures matched very well the *ab initio* results. In general, the new interatomic potential developed for this material seemed to give a reasonable description of the boundaries.

Ab initio computations also produced the electron localization function (ELF) which provided information about bonding across the interfaces. From the ELF, c-tilt and a-twist were seen to have significant covalent bonding across the interfaces whereas c-twist and a-tilt were more ionic. Strong covalent bonding is expected to improve the mechanical integrity of the boundary as well as to reduce thermal interfacial resistance.

Next, the interfacial thermal conductance σ_K was evaluated using nonequilibrium molecular dynamics. The Muller-Plathe method was used to produce a heat sink and a heat source on opposite sides of the boundaries. This temperature differential resulted in a discontinuity at the interfaces proportional to their thermal resistance. For our boundaries, c-tilt had the lowest thermal resistance. This result was not surprising since this boundary had the least reconstruction and is held together by strong covalent bonds. The highest interfacial thermal resistances was for a-tilt which was both more disordered and more ionic than the other boundaries. In general, however, all four boundaries had very low thermal resistances compared to estimates based on experimental data. That is not surprising since these boundaries are very crystalline, highly ordered, and free of impurities. Modern processing methods typically result in ceramics with much more disordered boundaries and with many impurities. These calculations show however that low energy structures with very favorable properties exist for these materials and might be produced by improved processing methods.

Finally, the effect of the grain boundary network on the bulk thermal conductivity of the material was considered. Grain boundaries are expected to reduce the thermal conductivity relative to its intrinsic, single crystal values. Estimates based on the Brick Layer Model indicate that boundaries with very low thermal resistance, such as the ones we considered, will produce a very small reduction in the intrinsic thermal

conductivity. To examine a more realistic situation, we performed a FEM thermal analysis using a microstructure obtained from an SEM image and also using more realistic thermal parameters. The FEM mesh was constructed directly on top of the image. From these computations, a significant reduction of thermal conductivity was seen with values much more comparable with experimental results.

IX. ACKNOWLEDGMENTS

J.W.L., T.H.S and C.W.B. are civil servants in the TS Division. M.S.D was supported under a NASA prime contract to ELORET Corporation. We benefited from discussions with Pawel Keblinski and Tapan Desai.

---

[1] L. Kaufman, E.V. Clougherty, "Investigation of Boride Compounds for Very High Temperature Applications, RTD-TRD-N63-4096, Part III, ManLabs Inc., Cambridge, MA, (March 1966)

[2] M.J. Gasch, D.T. Ellerby and S.M. Johnson, "Ultra High Temperature Ceramic Composites" in N.P. Bansal, ed., Handbook of Ceramic Composites, Boston: Kluwer Academic, p. 197-224, 2005

[3] W.G. Fahrenholtz, G.E. Hilmas, I.G. Talmy and J.A. Zaykoski, "Refractory Diborides of Zirconium and Hafnium", J. Am. Ceram. Soc. 90:1347, 2007

[4] S.M. Johnson, M.J. Gasch, T.H. Squire, J.W. Lawson, M.M. Stackpoole, M.I. Gusman, "Ultra high temperature ceramics: issues and prospects", Proc. 7th International Conference on High Temperature Ceramic Matrix Composites (HT-CMC7) 819-831, 2010

[5] W.S Williams, "Transition metal carbides, nitrides, and borides for electronic applications", JOM-Journal of the Minerals, Metals & Materials Society, 49:38, 1997; W.S Williams, "The thermal conductivity of metallic ceramic", JOM-Journal of the Minerals, Metals & Materials Society, 50:62, 1998

[6] H. Kinoshita, S. Otani, S. Kamiyama, H. Amano, I. Akasaki, J. Suda and H. Matsunami, "Zirconium Diboride (0001) as an Electrically Conductive Lattice-Matched

Substrate for Gallium Nitride", Jpn. J. Appl. Phys. 40:L1280, 2001

[7] J.W. Zimmermann, G.E. Hilmas, W.G. Fahrenholtz, R.B. Dinwiddie, W.D. Porter and H. Wang, "Thermophysical Properties of ZrB_2 and ZrB_2SiC Ceramics", J. Am. Cerm. Soc. 91:1405, 2008

[8] L. Zhang, D.A. Pejakovic, J. Marschall and M. Gasch, "Thermal and electrical transport properties of spark plasma-sintered HfB_2 and ZrB_2 ceramics", J. Am. Cerm. Soc., in press, 2011

[9] M.S. Daw, J.W. Lawson and C.W. Bauschlicher, "Interatomic potentials for Zirconium Diboride and Hafnium Diboride", Comp. Mat. Sci. 50:2828, 2011

[10] J.W. Lawson, M.S. Daw and C.W. Bauschlicher, "Lattice thermal conductivity ZrB_2 and HfB_2 from atomistic simulations", J. App. Phys. 11:083507, 2011

[11] J. Perdew, K. Burke, and M. Ernzerhof, Phys. Rev. Lett. 77:3865, 1996

[12] G. Kresse and J. Hafner, Phys. Rev. B 47 , 558 (1993); ibid. 49 , 14251 (1994); G. Kresse and J. Furthmller, Comput. Mat. Sci. 6 , 15 (1996); G. Kresse and J. Furthmller, Phys. Rev. B 54 , 11169 (1996); G. Kresse and J. Hafner, J. Phys.: Condens. Matt. 6 , 8245 (1994); G. Kresse and D. Joubert, Phys. Rev. B 59:1758, 1999

[13] A. D. Becke and K. E. Edgecombe, "A simple measure of electron localization in atomic and molecular systems", J. Chem. Phys. 92: 53975403, (1990)

[14] A. Savin, O. Jepsen, J. Flad, O.K. Andersen, H. Preuss and H.G. von Schnering, "Electron localization in solid-state structures of the elements the diamond structure", Angewandte Chemie-International Edition in English 31: 187188, (1992)

[15] S. Plimpton, "Fast Parallel Algorithms for Short-Range Molecular Dynamics", J. Comp. Phys. 117:1, 1995

[16] F. Muller-Plathe, "A simple nonequilibrium molecular dynamics method for calculating the thermal conductivity", J Chem Phys, 106:6082, 1997; M. Zhang, E. Lussetti, L.E.S de Souza and F. Muller-Plathe, "Thermal Conductivities of Molecular Liquids by Reverse Nonequilibrium Molecular Dynamics", J Phys Chem B, 109:15060-15067, 2005

[17] A. Maiti, G.D. Mahan and S.T. Pantelides, "Dynamical simulations of nonequilibrium processes - heat flow and the Kapitza resistance across grain boundaries", Solid State

Comm. 102:517, 1997

[18] P.K. Schelling, S.R. Phillpot and P. Keblinski, "Kapitza conductance and phonon scattering at grain boundaries by simulations", J. App. Phys. 95:6082, 2004

[19] A.C.E. Reid, S.A. Langer, R.C. Lua, V.R. Coffman, S.I. Haan, and R.E.Garca, "Image-based finite element mesh construction for material microstructures", Comp. Mat. Sci. 43:989, 2008

[20] MSC Software Corporation, Marc Version 2008r1, 2 MacArthur Place, Santa Ana, CA 92707

[21] S. Hazanov and C. Huet, "Order relationships for boundary conditions effect in heterogeneous bodies smaller than the representative volume", J. Mech. Phys. Solids 42:1995, 1994

[22] J.P. Crocombette and L. Gelebart, "Multiscale modeling of the thermal conductivity of polycrystalline silicon carbide, J. Applied Physics 106:083520, 2009

[23] T. Kanit, S. Forest, I. Galliet, V. Mounoury and D. Jeulin, "Determination of the size of the representative volume element for random composites: statistical and numerical approach", Int. J. Solids and Structures 40:3647, 2003

[24] D.H. Warrington, "The coincidence site lattice (CSL) and grain boundary (DSC) dislocations for the hexagonal lattice", J. de Physique, C4, 1975, vol 36, p.C4-87

[25] D. Farkas, "Grain-boundary structures in hexagonal materials: coincident and near coincident grain boundaries", Met. and Mat. Trans. A 25A:1337, 1994

[26] A.P. Sutton and R.W. Balluffi, *Interfaces in Crystalline Materials*, (Clarendon, New York, 1995)

[27] E.C. Dickey, X. Fan and S.J Pennycook, "Structure and Chemistry of Yttria-Stabilized Cubic-Zirconia Symmetric Tilt Grain Boundaries", J. Am. Ceram. Soc. 84:1361, 2001

[28] J.P. Buban, K. Matsunaga, J Chen, N. Shibata, W.Y. Ching, T. Yamamoto, and Y. Ikuhara, "Grain Boundary Strengthening in Alumina by Rare Earth Impurities", Science 311:212, 2006

[29] S. von Alfthan, K. Kaski and A.P. Sutton, "Order and structural units in simulations of twist grain boundaries in silicon at absolute zero", Phys. Rev. B 74:134101, 2006

[30] A.L.-S. Chua, N.A. Benedek, L. Chen, M.W. Finnis and A.P. Sutton, "A genetic algo-

rithm for predicting the structures of interfaces in multicomponent systems", Nature Mat. 9:418, 2010

[31] R. Grantab, V.B. Shenoy and R.S. Ruoff, "Anomalous strength characteristics of tilt grain boundaries in graphene", Science 330:946, 2010

[32] O.V. Yazyev and S.G Louie, "Topological defects in graphene: dislocations and grain boundaries", Phys. Rev. B 81:195420, 2010

[33] J.W. Lawson, C.W. Bauschlicher and M.S. Daw, "Ab initio calculations of electronic, mechanical and thermal properties of ZrB_2 and HfB_2" J. Am. Ceram. Soc. 94:3494, 2011

[34] Z. Mao, S.B. Sinnott and E.C. Dickey, "*Ab initio* calculations of pristine and doped Zirconia $\Sigma 5$ (310)/[001] tilt grain boundaries", J. Am. Ceram. Soc. 85:1594, 2002

[35] M. Kohyama, "Computational studies of grain boundaries in covalent materials", Modelling Simul. Mater. Sci. Eng. 10:R31, 2002

[36] D.S. Smith, S. Fayette, S. Grandjean, C. Martin, R. Telle and T. Tonnessen, "Thermal Resistance of Grain Boundaries in Alumina Ceramics and Refractories", J. Am. Ceram. Soc. 86:105 (2003)

[37] D.G. Cahill, W.K. Ford, K.E. Goodson, G.D. Mahan, A. Majumbar, H.J. Maris, R. Merlin, S.R. Philpot, "Nanoscale thermal transport", J. App. Phys. 93:793 (2003)

	Ab Initio		DLB/Pot 1		
	γ (meV/Å^2)	Δ_z (Å)	γ (meV/Å^2)	Δ_z (Å)	σ_K $(GW/(m^2 \cdot K))$
c-tilt	153(369)	-	112(238)	-	1.77
c-twist	157(375)	0.29	111(258)	0.29	0.58
a-tilt	227(1040)	-	107(1380)	-	0.38/0.31
a-twist	212(1230)	-	118(1430)	-	0.55/0.53

TABLE I: Energetics and thermal conductance for ZrB_2 grain boundary structures from empirical potentials (DLB/Pot 1) and *ab initio*/DFT. Units for γ are meV/Å^2, Δ_z are Å and σ_K are $GW/(m^2 \cdot K)$. Unrelaxed quantities are in parenthesis.

κ_{eff}	Vertical	Horizontal	
FEM/Transient	18		18
FEM/UTG	17.5	16.2	16.8
FEM/UHF	16.7	15.9	16.3
BLM			10
ROM			44
Exp.			22

TABLE II: Effective thermal conductivity values $(W/(m \cdot K))$ for the SEM microstructure from FEM computations, the Brick Layer Model (BLM), the Rule of Mixtures (ROM) and the experimental value [7]. FEM computations are obtained from a transient method as well as two steady state approaches using the uniform temperature gradient UTG boundary condition and the uniform heat flux UHF boundary condition. Vertical and horizontal give the direction of heat transport. The last column gives the average if the result is direction dependent.

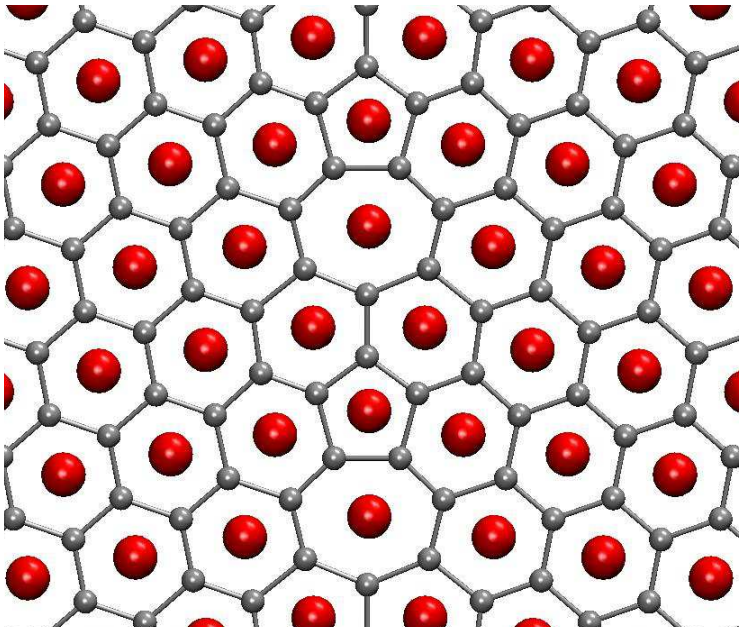

FIG. 1: Atomic structure of $\Sigma 7$ symmetric c-axis tilt boundary for ZrB_2 with Zr (red) and B (gray) atoms shown. The boundary contains 5-7 membered ring pairs separated by hexagonal rings. This structure is similar to ones proposed for graphene.

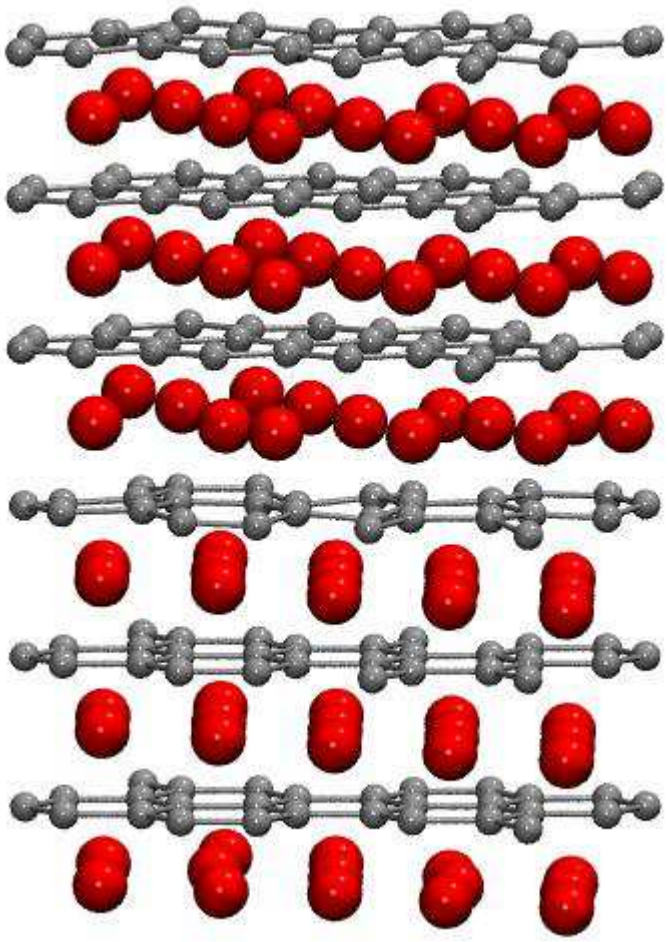

FIG. 2: Atomic structure of $\Sigma 7$ symmetric c-axis twist boundary for ZrB_2 with Zr (red) and B (gray) atoms shown. A layer of Zr has been shifted relative to a B layer resulting in crumpling.

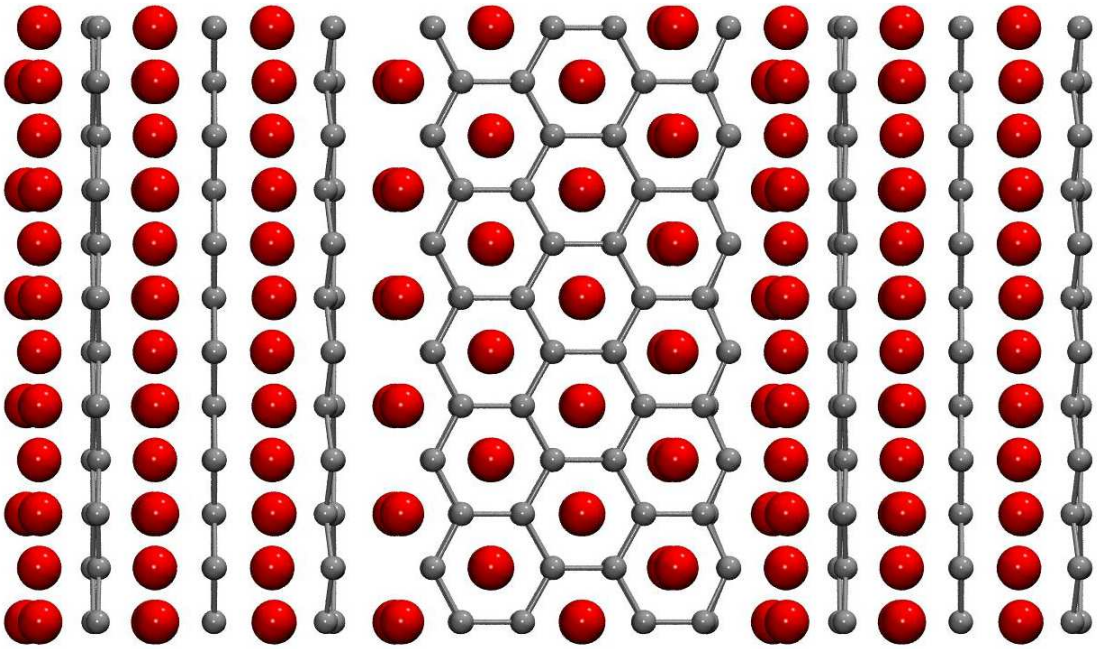

FIG. 3: Atomic structure of 90°, near coincidence, asymmetric a-axis tilt boundary for ZrB_2 with Zr (red) and B (gray) atoms shown. Unit cell has two boundaries designated Left and Right. A rotated view of this boundary can be seen in Fig. 7.

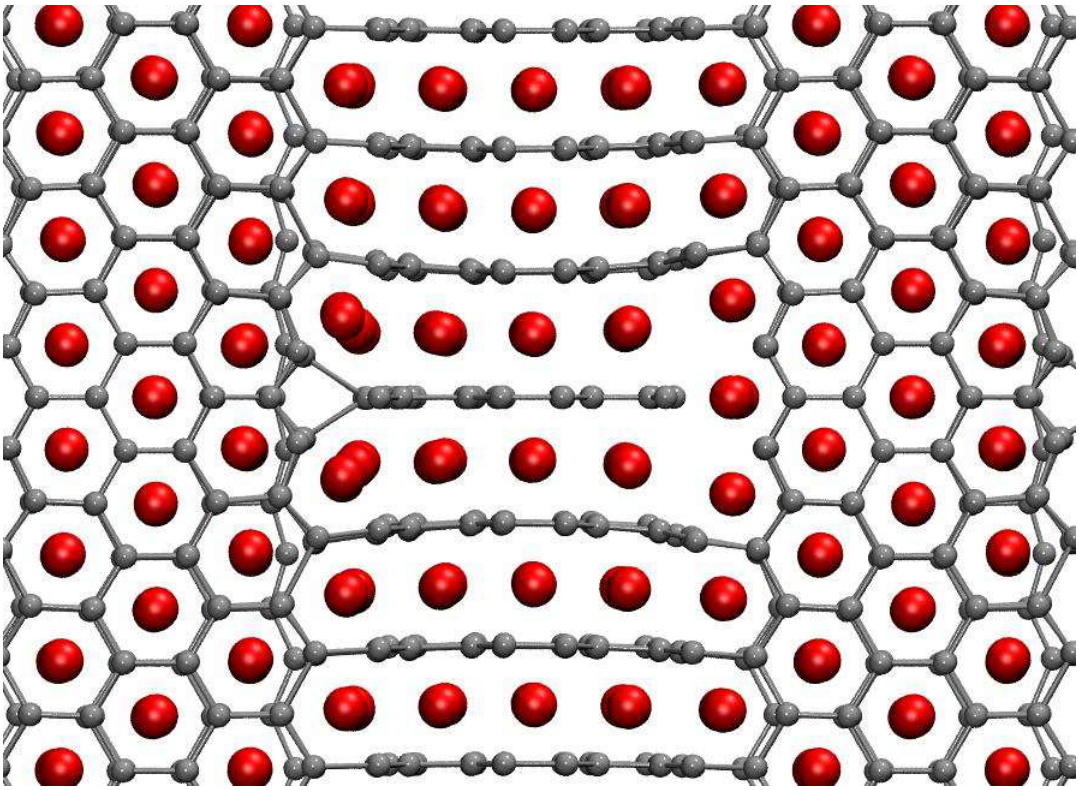

FIG. 4: Atomic structure of 90°, near coincidence, asymmetric a-axis twist boundary for ZrB_2 with Zr (red) and B (gray) atoms shown. Unit cell has two boundaries designated Left and Right. Significant reconstruction makes this the most disordered boundary.

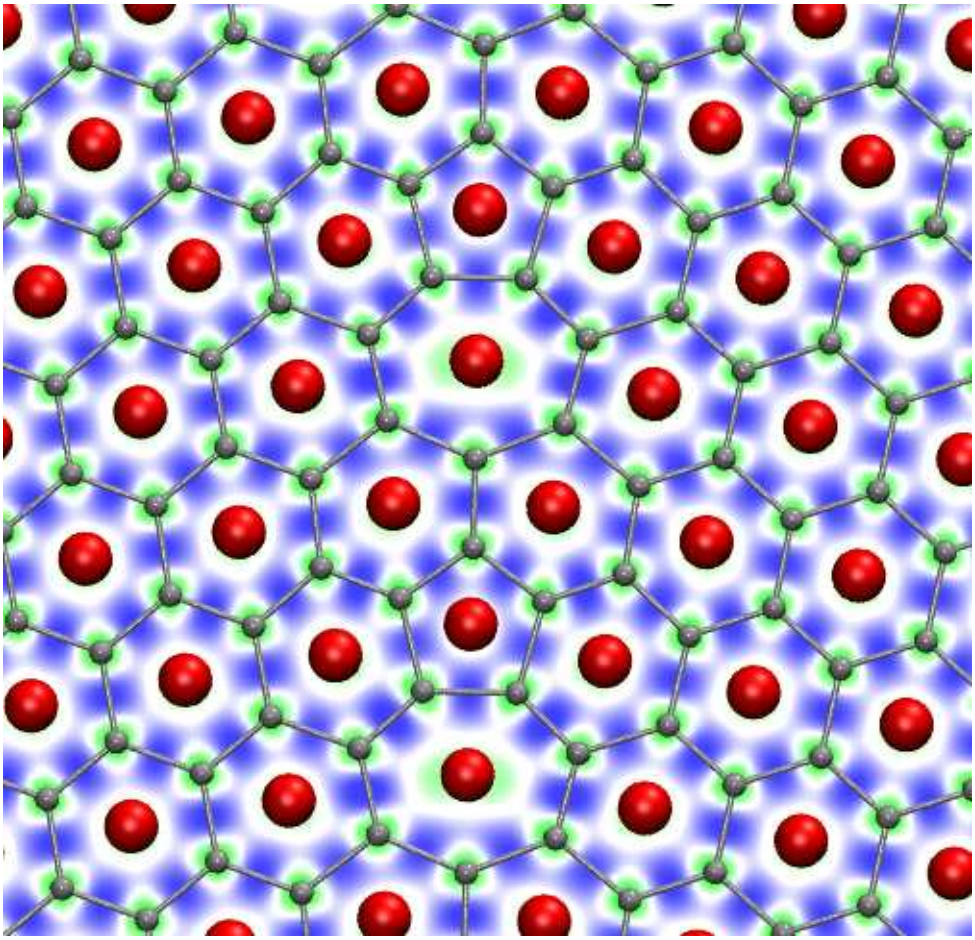

FIG. 5: ELF for the c-tilt boundary. Blue is high ELF and green is low ELF. The figure shows a cut through a B plane. High ELF between B atoms indicate strong, highly directional covalent bonds form across the interface.

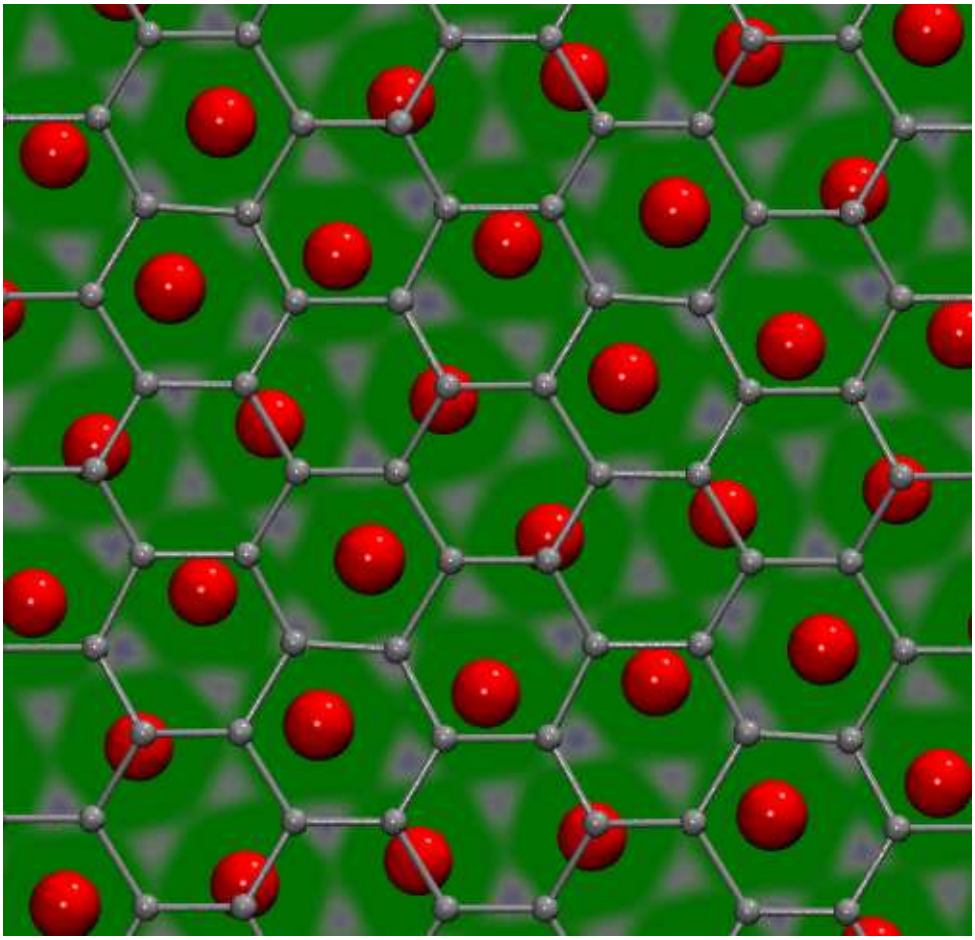

FIG. 6: ELF for the c-twist boundary. Blue is high ELF and green is low ELF. The twist results in the misalignment of the Zr and B planes. The figure shows a cut through a Zr plane where the ELF is low and less directional than Fig. 5. ELF accumulation points can be seen forming 6-membered rings around the Zr atoms.

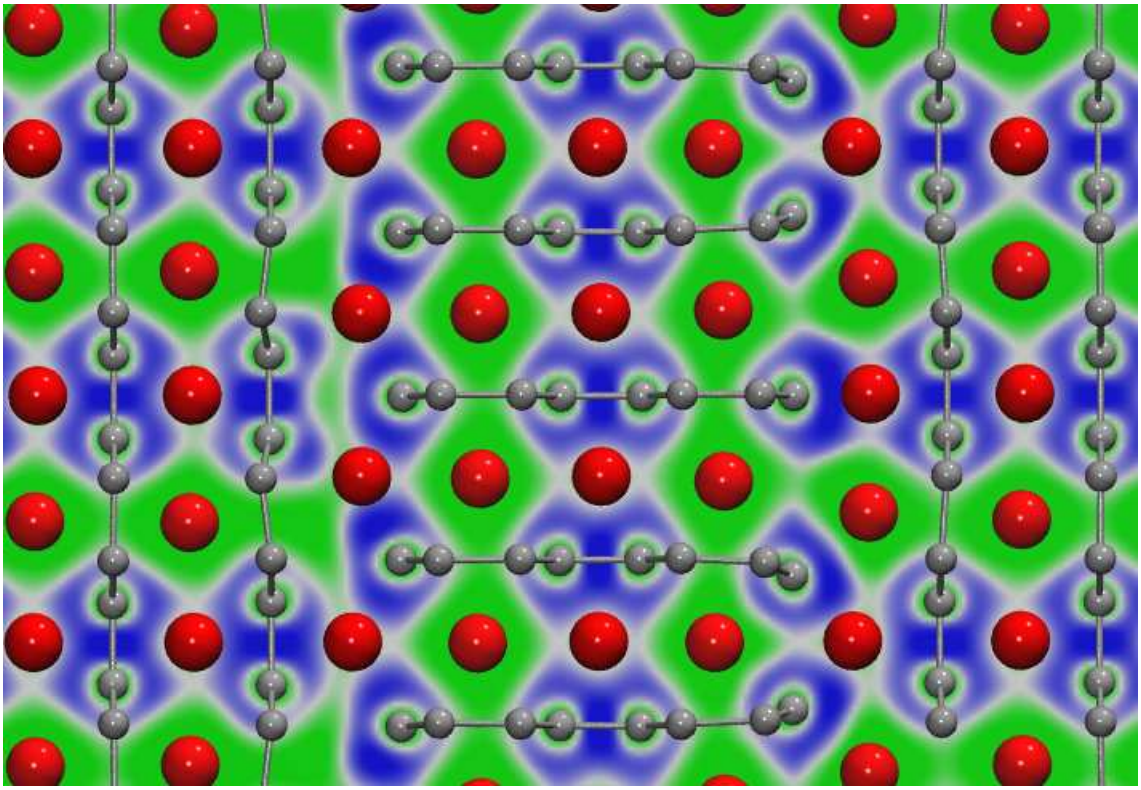

FIG. 7: ELF for the a-tilt boundary. Blue is high ELF and green is low ELF. The boundary is asymmetric. The figure is a cut with maximum ELF in the boundary. Interacting pockets of high ELF can be seen due to B pairs.

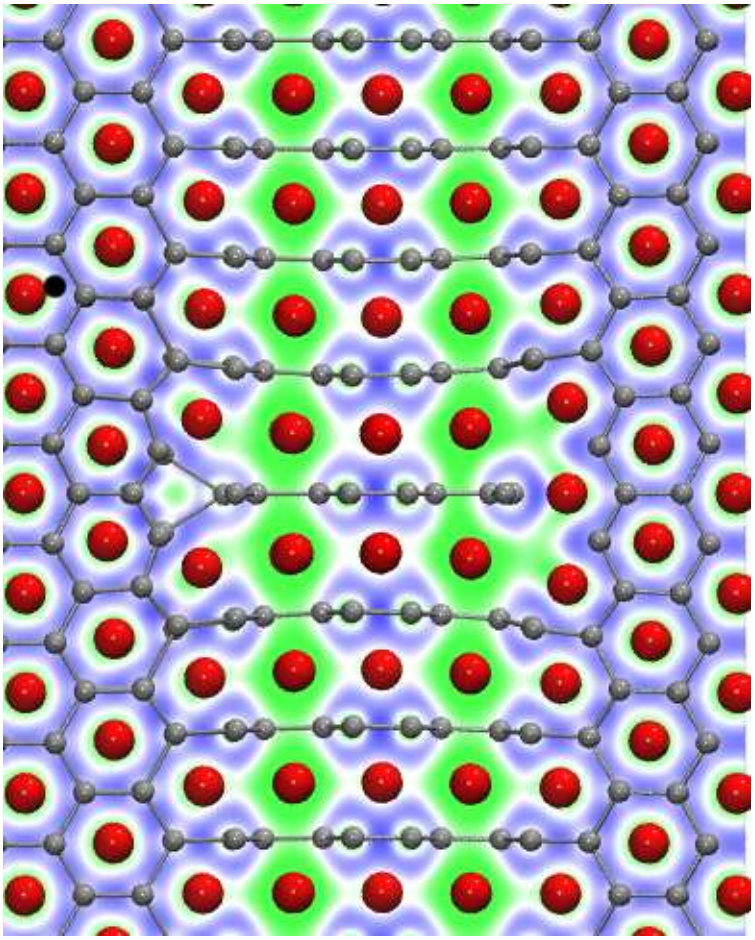

FIG. 8: ELF for the a-tilt boundary. Blue is high ELF and green is low ELF. The boundary is asymmetric. The figure is a cut with maximum ELF in the boundary. Significant and complex B bonding can be seen across the boundary. Formation of 4-membered rings is observed.

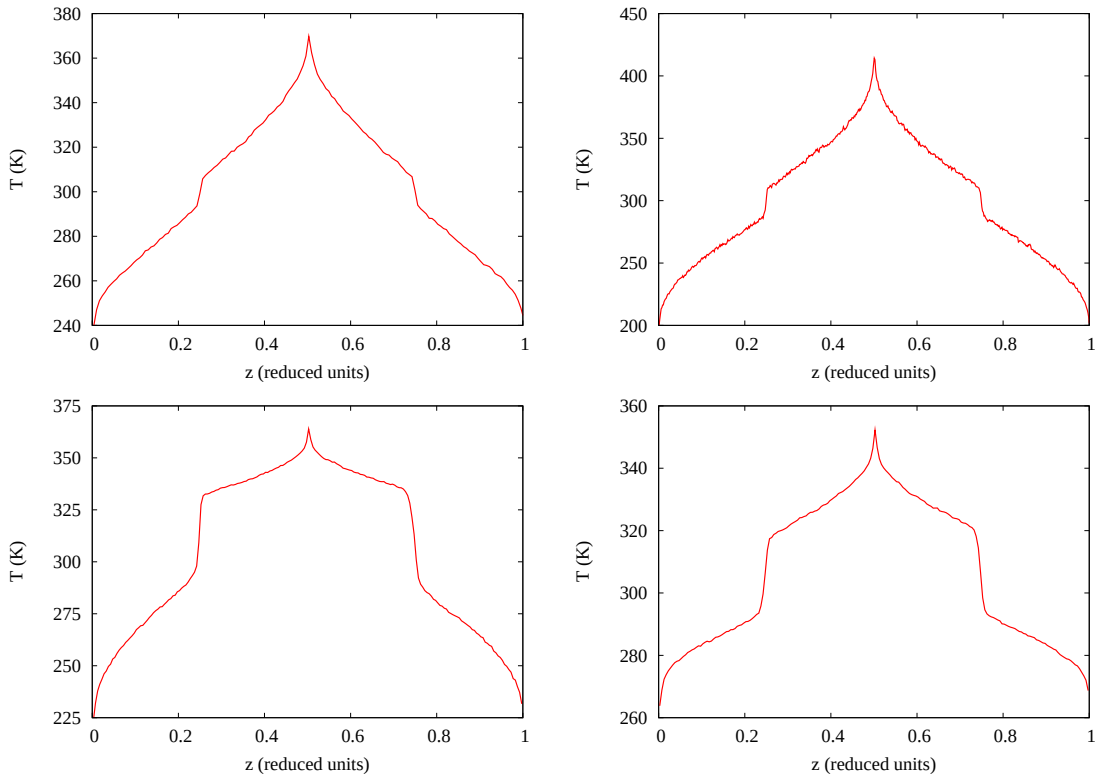

FIG. 9: Temperature profiles versus simulation cell distance normal to the grain boundaries for c-tilt (upper left), c-twist (upper right), a-tilt (lower left), and a-twist (lower right). Cell distance is in reduced units. Grain boundaries are positioned at $z = .25$ and $z = .75$. Temperature discontinuity is related to the interface thermal resistance σ_K.

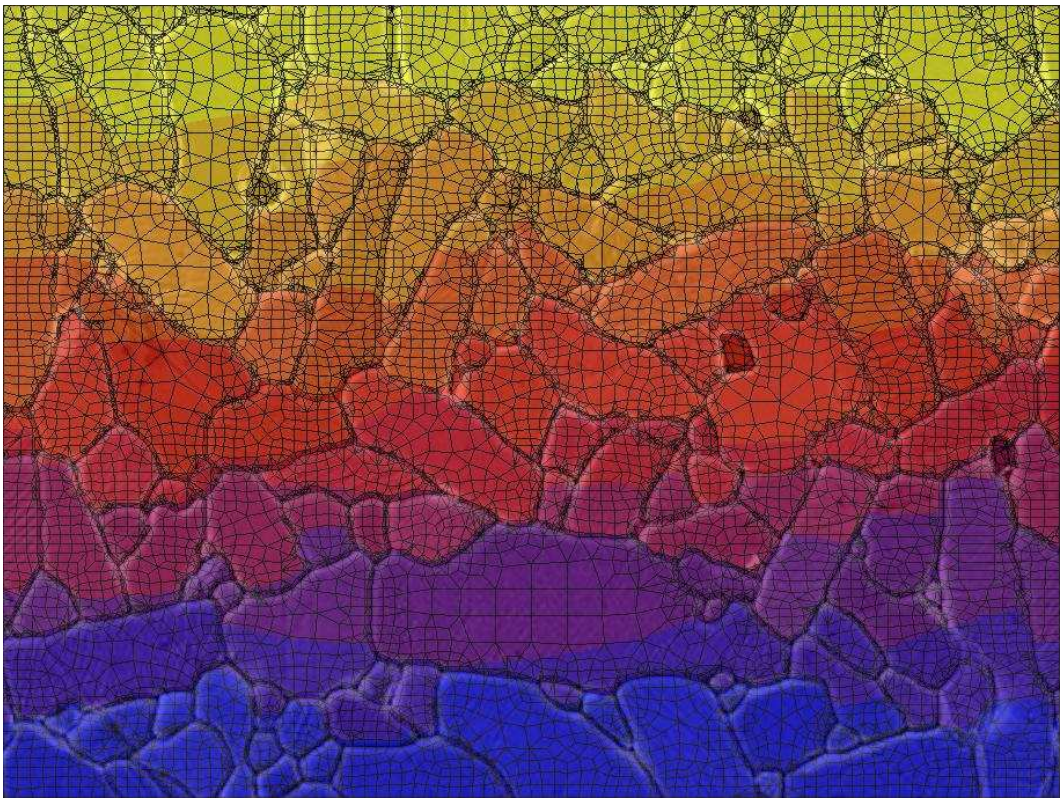

FIG. 10: Finite element thermal analysis for a ZrB_2 microstructure. The FEM mesh was constructed on top of an SEM image of ZrB_2 [3]. The figure shows the original image, the FEM mesh, and constant temperature contours from a steady state thermal solution. Yellow is high temperature and blue is low temperature.

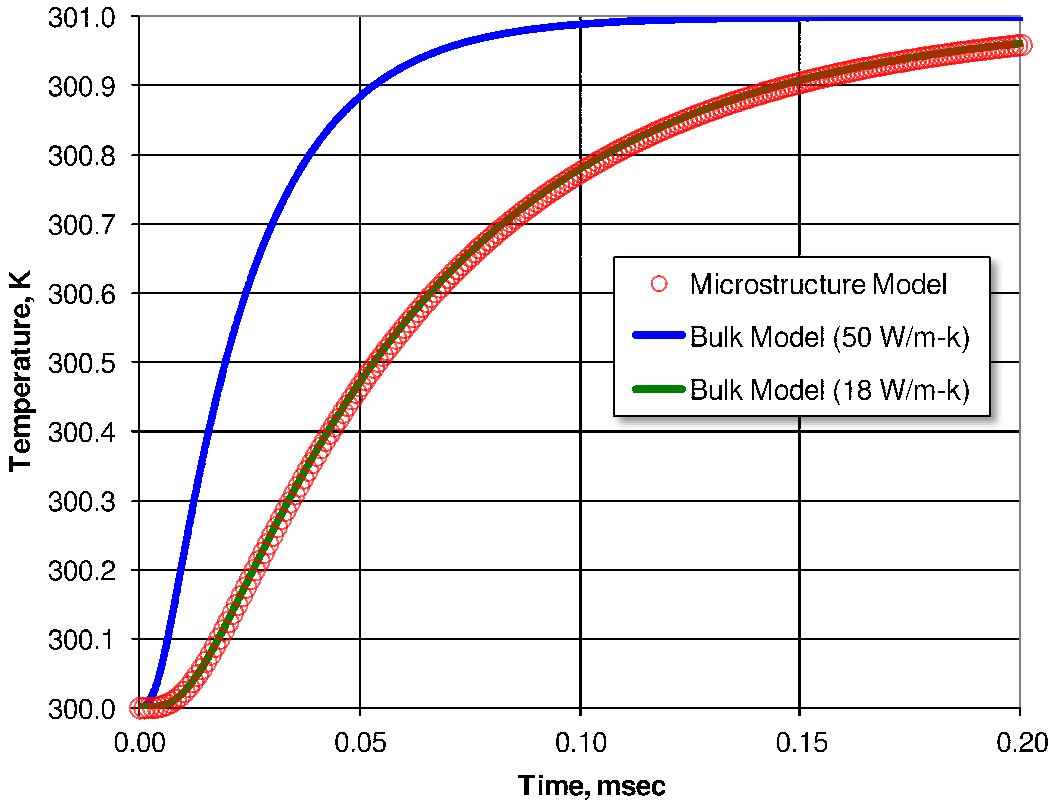

FIG. 11: Transient temperature response at the bottom of the model after a flux has been applied to the top as a function of time. The effective temperature of the model is determined by fitting the solution to an equivalent, bulk, reference material. A bulk system with the intrinsic thermal conductivity κ_0 shows the reduction due to interfacial resistance.